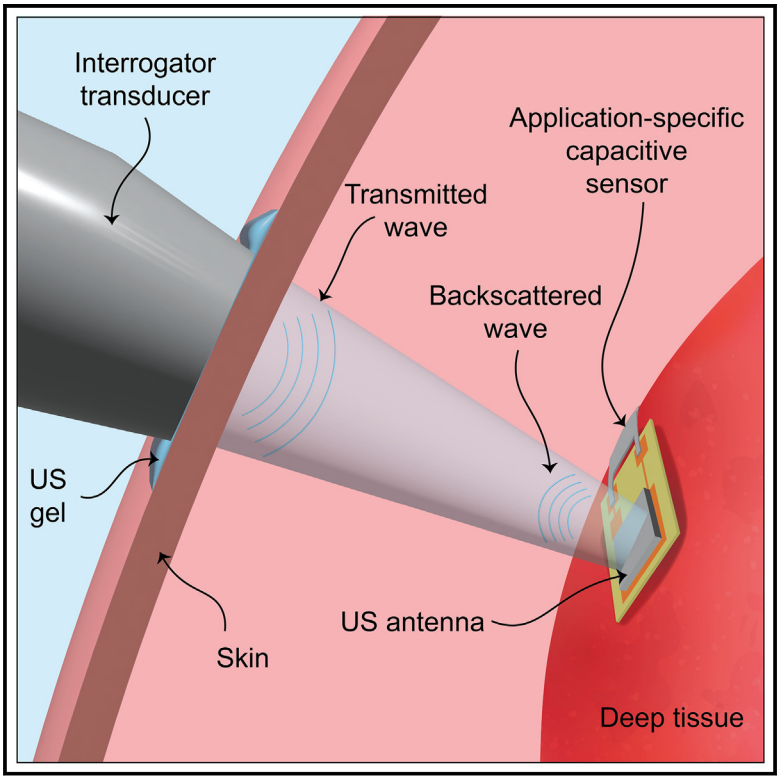
Device

Article

Passive ultrasonic communication link for deep-tissue sensor implants

Graphical abstract



Highlights

- Passive ultrasonic communication method eliminates the need for implant electronics
- Enables wireless deep-tissue sensing using a simple piezoelectric antenna
- Demonstrated real-time pressure monitoring at 5 cm depth
- Compatible with any capacitive implantable sensor for broad medical applications

Authors

Umut Can Yener, Alp Timucin Toymus, Kivanc Esat, Mehdi Alem, Levent Beker

Correspondence

lbeker@ku.edu.tr

In brief

Yener et al. present a passive, frequency-based ultrasonic communication system that enables wireless sensor data transmission without electronics. Using a simple piezoelectric antenna and capacitive sensing, the system demonstrates precise pressure monitoring at a clinically relevant depth. This approach paves the way for simplified and broadly applicable implantable monitoring devices.

2 Explore
Early prototypes with exciting performance and new methodology

Yener et al., 2025, Device *3*, 100755
July 18, 2025 © 2025 The Author(s). Published by Elsevier Inc.
https://doi.org/10.1016/j.device.2025.100755

CellPress

Device

CellPress
OPEN ACCESS

Article

Passive ultrasonic communication link for deep-tissue sensor implants

Umut Can Yener,[1] Alp Timucin Toymus,[1] Kivanc Esat,[2] Mehdi Alem,[2] and Levent Beker[1,3,4,*]
[1]Department of Mechanical Engineering, Koç University, Rumelifeneri Yolu, Sarıyer, Istanbul 34450, Turkey
[2]Zurich Instruments, Ltd., Technoparkstr. 1, 8005 Zurich, Switzerland
[3]Department of Biomedical Sciences and Engineering, Koç University, Rumelifeneri Yolu, Sarıyer, Istanbul 34450, Turkey
[4]Lead contact
*Correspondence: lbeker@ku.edu.tr
https://doi.org/10.1016/j.device.2025.100755

THE BIGGER PICTURE Wireless communication is crucial for medical implants, enabling real-time monitoring of deep-tissue physiological conditions without invasive procedures. However, existing electromagnetic-wave-based communication methods face limitations due to high signal attenuation, while ultrasonic methods require application-specific integrated circuits or metamaterial sensors. In this work, the authors introduce a frequency-based, passive, electronics-free ultrasonic communication method that overcomes the limitations of existing methods. This technology can aid deep-tissue sensing by allowing non-invasive data transmission for medical applications such as pressure monitoring, organ health assessment, and chronic disease management.

SUMMARY

Wireless communication is critical for non-invasive *in situ* monitoring of vital signs in deep tissues. Electromagnetic-wave-based communication methods suffer from high attenuation and limited penetration in biological tissues. Wireless ultrasonic links can solve these shortcomings but typically require highly customized and complex designs for the implant electronics or rely on physical changes in implanted metamaterials. Here, we report a wireless, passive, frequency-based, and electronics-free ultrasonic communication method for deep-tissue sensor implants. The device consists of a piezoelectric crystal used as the ultrasonic antenna with a simplified design and can be integrated with any capacitive implantable sensor. We demonstrate the applicability of the passive communication method using a commercial pressure sensor at a depth of 5 cm, revealing a sensitivity of 5.83 pF/kPa below 20 kPa.

INTRODUCTION

Many medical conditions occur deep within the tissue, which makes it difficult to monitor and diagnose based on external measurements.[1–3] Medical imaging techniques, such as ultrasonography and magnetic resonance imaging, are helpful in getting clinically relevant information from deep tissues non-invasively, but they are not suitable for cases where continuous *in situ* monitoring is necessary.[4,5] For such cases, it is possible to monitor signs deep within the body using invasive instruments like catheters.[6–8] Nonetheless, these alternatives are restricted to clinical settings, require trained personnel, and are costly for the healthcare system. Moreover, the invasive nature of these techniques holds the risk of causing discomfort, bleeding, scarring, and bacterial infections.[9–13] As an alternative to the clinically available invasive measurement techniques, medical implants have the ability to sense signals subcutaneously. Unlike early examples that use percutaneous wired connections to external devices, recent implantable devices use wireless power- and data-transferring technologies such as inductive coupling,[14–17] magnetic resonance coupling,[18–20] near-field communication,[21–23] and Bluetooth.[24–26] However, the high tissue attenuation and low penetration depth associated with electromagnetic (EM) waves either limit the implantation depth for these devices or necessitate wired connections between the deeply implanted sensor and subcutaneously implanted antenna (Figure S1), which introduce similar risks associated with wired connections.[27,28]

Transferring power and data via ultrasound (US) has recently attracted attention for deep-tissue implantable devices. US offers millimeter (below 1.5 MHz) and submillimeter (above 1.5 MHz) wavelengths at the diagnostic US frequency range, which achieves better coupling with miniaturized implants when compared to EM waves (wavelength of 25 mm at 2 GHz). Additionally, US offers lower attenuation in soft tissues ($\sim$1.5 dBcm^{-1} at 2 MHz for US and $\sim$10 dBcm^{-1} at 2 GHz for EM), which results in higher penetration depth and less tissue heating.[29] For these

This is an open access article under the CC BY-NC-ND license (http://creativecommons.org/licenses/by-nc-nd/4.0/).

reasons, several studies have demonstrated implantable devices with US power and data links[30–38] for various applications, including wireless recording of the nervous system and real-time tissue oxygenation and temperature monitoring. However, most devices with US data links rely on the use of electronic components for power harvesting and active digital communication. As a result, these devices consist of capacitor elements to store energy, rectifier circuits to harvest power, and custom integrated circuit (IC) chips to modulate sensor data to the backscattered US waves and switch between powering and data transferring modes, which lead to heavily customized and complex implant electronics design and fabrication. Alternatively, several studies have demonstrated electronics-free ultrasonic communication using implanted metamaterials.[39–42] However, these devices cannot be used for general-purpose communication methods as they rely on application-specific deformations or property changes on the metamaterials. A recent study has demonstrated a passive US pressure sensing device leveraging the amplitude changes in impedance.[43] However, amplitude-based approaches have limited applicability as they are highly susceptible to disturbances in the acoustic coupling. Therefore, a frequency-based alternative would be an important step toward reliable passive ultrasonic communication (PUC).

Here, we present a frequency-based PUC method to enable electronics-free data transfer from deep-tissue capacitive sensor implants for real-time monitoring applications. The implantable device consists of an ultrasonic antenna comprised of a single piezoceramic crystal and an implantable capacitive sensor. The PUC method leverages the changes in the resonance characteristics of the ultrasonic antenna due to the sensor's capacitance, which can be captured by an external interrogator ultrasonic transducer, thereby eliminating the necessity for custom IC chips and power-harvesting circuits and considerably simplifying the implant design. The electronics-free communication system is demonstrated *in vitro* with a commercial pressure sensor and is capable of detecting pressures in a clinically relevant range. The system presents a promising ultrasonic communication method for deep-tissue applications that can be integrated with any implantable capacitive sensor.

RESULTS AND DISCUSSION

Device design and working principle

The operating principle of the wireless and PUC method is shown in Figure 1A. The passive link is achieved between an external interrogator transducer and a piezoceramic US antenna connected to a capacitive sensor. The interrogator transducer transmits US waves, which travel through the soft tissue and get reflected by the implantable US antenna along with the surrounding soft-tissue boundaries. The backscattered echo of the incident pulse is captured by the interrogator transducer and converted to electrical signals to extract the sensor readings wirelessly.

An electrical equivalent circuit can be constructed for the US antenna and capacitive sensor, which comprises a Butterworth-van Dyke PZT model and a single capacitor, respectively (Figure 1B). Monitored signs cause capacitive changes (C_L) in the implantable sensor. These changes directly affect the resonance characteristics of the whole device[44] (Note S1). In particular, the anti-resonance frequency of the system shifts in correlation with the changes in the capacitive load that is connected to the US antenna (Figures 1C, S2, and S3). At this frequency, the incoming wave backscatters less, resulting in reduced signal amplitude captured by the interrogator transducer. This effect is determined by the acoustic reflection coefficient, as described in Note S2. Therefore, exciting the US antenna by an external transducer at frequencies near the anticipated anti-resonance frequency and recording the backscattered US waves result in a spectrum where the minimum point reveals the anti-resonance frequency of the implanted system, which can be used to find the capacitive load and, consecutively, the deep-tissue measurements performed by the implantable capacitive sensor (Figure 1D).

The exploded view of the fabricated ultrasonic antenna is presented in Figure 1E. The device consists of a millimeter-scale piezoceramic, a 200-μm-thick flexible electronic board substrate that facilitates the electrical connections, and a biocompatible polymer coating for chemical and electrical isolation. Moreover, an air-backing design approach is adopted by creating an air cavity at the back of the PZT crystal to reduce mechanical damping, which helps the PZT crystal vibrate more freely. Additionally, the capacitive pressure sensor is shown soldered to the fabricated antenna device. Figure 1F shows the fabrication flow of the device. First, the thin conductive substrate is patterned and cut, then the PZT crystal is soldered on the substrate, and finally, the device is encapsulated for electrical and chemical isolation.

Considering the wavelength for efficient coupling to millimeter-scale US antenna and frequency-dependent attenuation of the US in soft tissues,[45] the aspect ratio and thickness of the PZT crystal were determined such that the resonance and anti-resonance frequencies of the thickness mode operation are around 2 MHz, with a 5 × 7 mm^2 footprint and a total volume of 16 mm^3 (Figure 1G).

Electrical and mechanical device characterization of the device

Figure 2A shows a detailed Leach electroacoustic equivalent circuit model (ECM) of the ultrasonic antenna where the PZT crystal, backing layer, and acoustic medium are modeled as lossy transmission lines. The Leach model was selected due to its compatibility with SPICE (also known as [aka] simulation program with IC emphasis), unlike KLM (Krimholtz, Leedom, and Matthaei), Mason, or Redwood circuit models, which consist of either frequency-dependent transformers or negative-valued capacitive elements.[46–48]

The electrical impedance measurement of the device was compared to the Leach model simulation results in Figure 2B. The measurement shows an anti-resonance frequency of 2.3 MHz, as expected. Although the simulation results match the measurement at the anti-resonance frequency, resonance profiles do not match, as the thickness resonance of the PZT crystal mixes with other vibration modes due to using unconventional PZT dimensions[49] (see Note S3 for a detailed discussion). Nevertheless, the model-measurement mismatch is not crucial, as the key is the precise detection of small changes in the capacitive

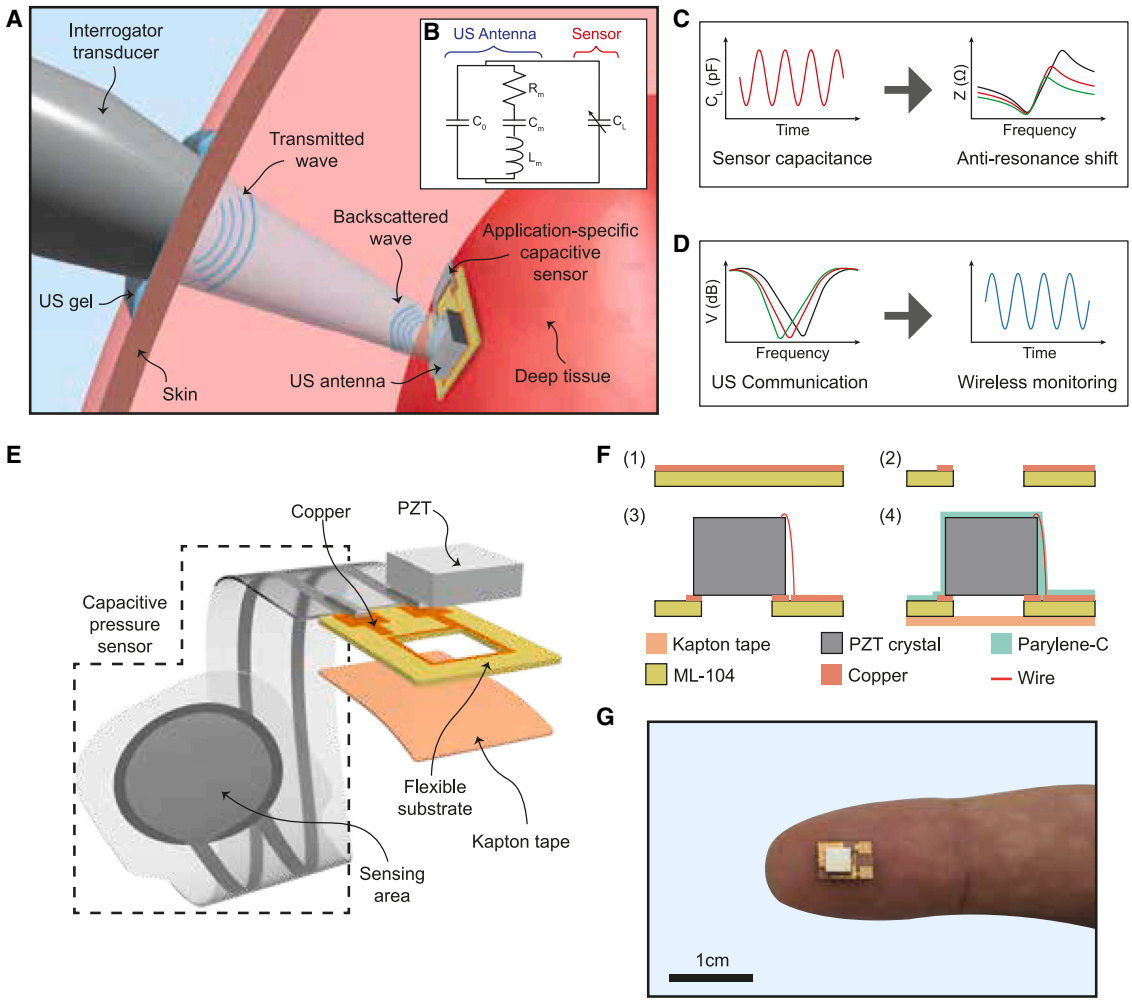


Figure 1. Device design and working principle

(A) Schematic of the passive ultrasonic communication method. The ultrasonic antenna is placed on a deep tissue, and the wireless communication link is established between the device and the external interrogator transducer.

(B) The simple equivalent circuit model of the implanted device. The ultrasonic antenna and capacitive sensor are represented by a Butterworth-van Dyke circuit and a capacitor, respectively.

(C) Deep-tissue measurements change the sensor capacitance, which directly affects the anti-resonance frequency of the device.

(D) Anti-resonance frequency shifts are detected wirelessly using the passive ultrasonic communication method. The shifts occurring in the frequency spectrum are translated into wireless sensor readings.

(E) Exploded view of the device showing the patterned flexible conductive substrate, piezoceramic antenna, and air-cavity encapsulation.

(F) The fabrication flow starts with an unpatterned conductive substrate (1), which is cut and patterned using laser micromachining (2). The PZT crystal is then soldered on the copper traces (3). As a last step, the air cavity is sealed using Kapton tape, and the device is encapsulated using Parylene-C (4).

(G) Optical image of the PUC device on a finger for size comparison before the top electrode is soldered.

load utilizing the anti-resonance frequency shifts. The measured and simulated effects of capacitive load on the impedance spectrum are shown in Figures 2C and 2D. Here, the thickness mode anti-resonance frequency decreases as the load capacitance connected to the US antenna increases.

The measured and simulated anti-resonance frequency shifts were compared in Figure 2E. The ultrasonic antenna was further characterized using an acoustic frequency sweep test, presented in Figure 2F, showing maximum acoustic pressure at 2.02 MHz, measured by a needle hydrophone 3 cm away from the antenna surface, which indicates that the resonance observed around 2 MHz is the thickness vibration mode of the antenna. The acoustic pressure field of the US antenna was measured using a motorized ultrasonic measurement system 3 cm away from the source (Figure 2G), revealing a −3 dB diameter of 9.4 mm.

Communication link characterization

Figure 3A shows the schematic block diagram of the communication hardware system. A duplexer is used to connect the interrogator transducer to the input and output channels of a lock-in amplifier (LIA), enabling transmit and receive operations from the

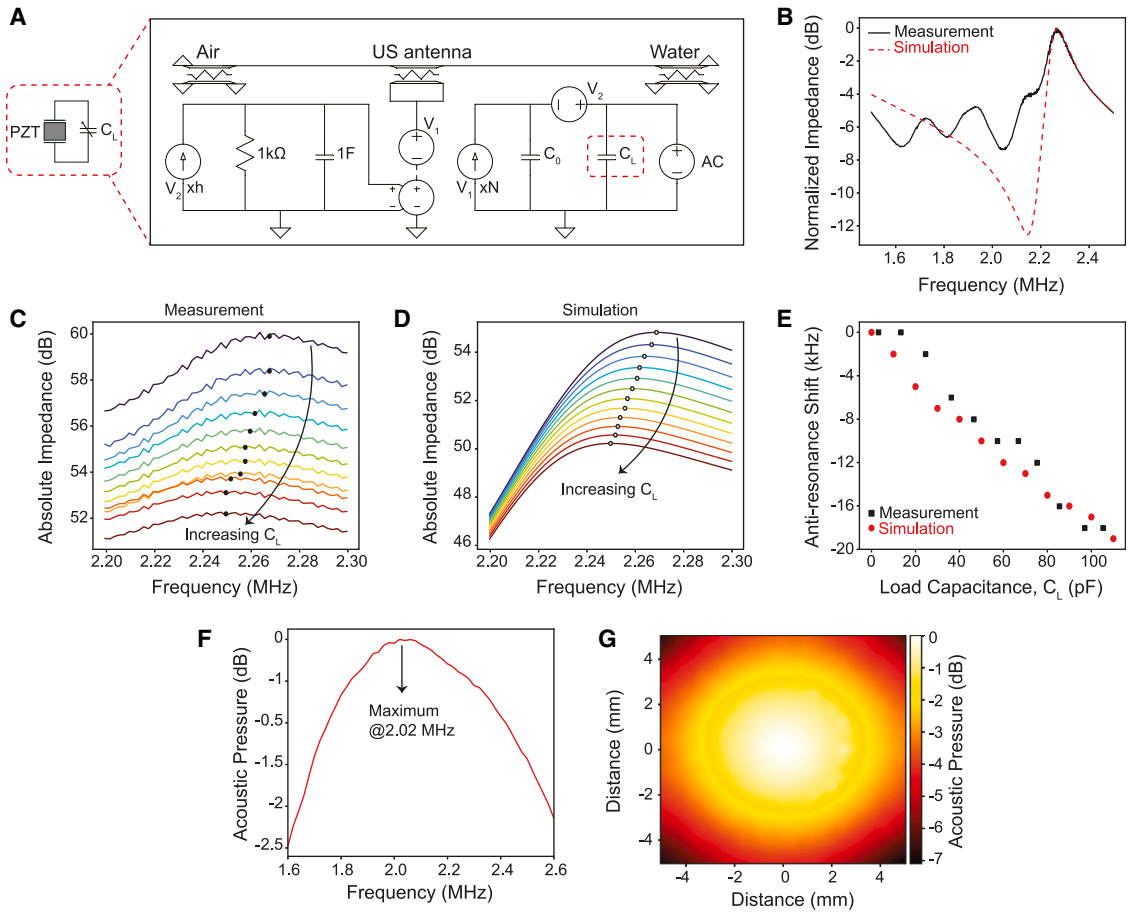


Figure 2. Electrical and mechanical device characterization of the device

(A) Schematic of the SPICE equivalent circuit model of the ultrasonic antenna in water constructed in LTspice software. The Leach model is used for its SPICE-friendly nature. The air-backing medium, PZT crystal, and acoustic medium are modeled as lossy transmission lines.

(B) Measured and simulated absolute electrical impedance of the US antenna. The resonance characteristics of the fabricated device do not match fully with the simulation due to unconventional PZT dimensions.

(C and D) Electrical impedance curves of the measured (C) and simulated (D) US antenna under various capacitive loads. The peaks in the impedance curves are anti-resonance frequencies.

(E) Anti-resonance frequency shifts for varying capacitive loads. The measurement results show good agreement with the simulation.

(F) Acoustic frequency sweep test results of the US antenna showing peak acoustic pressure level at 2.02 MHz.

(G) Acoustic pressure field of the US antenna is measured by a needle hydrophone at a depth of 3 cm.

same interrogator transducer and, hence, facilitating pulse-echo measurements. The internal oscillator of the LIA determines the frequency of the generated excitation signals, which are then amplified by a radio frequency (RF) amplifier. To demodulate the echo signal, the LIA mixes it with a sinusoidal waveform at the same frequency as the excitation signal and applies the outcome to a low-pass filter, which forms the envelope of the unprocessed time-domain signal. An unprocessed pulse-echo waveform and its demodulated form are shown in Figure 3B. After the signal is demodulated, the LIA obtains the average signal level within the demodulator trigger interval. These pulse-echo measurements are repeated for each frequency until the entire frequency interval is swept. The minimum point in the resulting frequency-dependent amplitude spectrum reveals the minimum acoustic reflection point, which is the anti-resonance frequency of the US antenna.

To confirm the effect of the presence of the US antenna, sweep operations were performed with and without the US antenna in front of the interrogator transducer. The resulting sweeper spectrum shows a clear valley when the US antenna is in front of the commercial interrogator transducer. In contrast, when a thin metal object is placed instead of the US antenna, the previously observed valley disappears (Figure 3C). Moreover, the effect of the excitation signal duration and amplitude were analyzed. The results depicted in Figure 3D show that the valley of the sweep profile gets more pronounced as the signal duration increases. On the other hand, the amplitude of the excitation signal has no noticeable effect on the performance (Figure S4).

The PUC method was further analyzed for varying interrogator-antenna distances, as shown in Figure 3E. The distance only slightly affects the communication method results, and it can be entirely compensated since the distance information

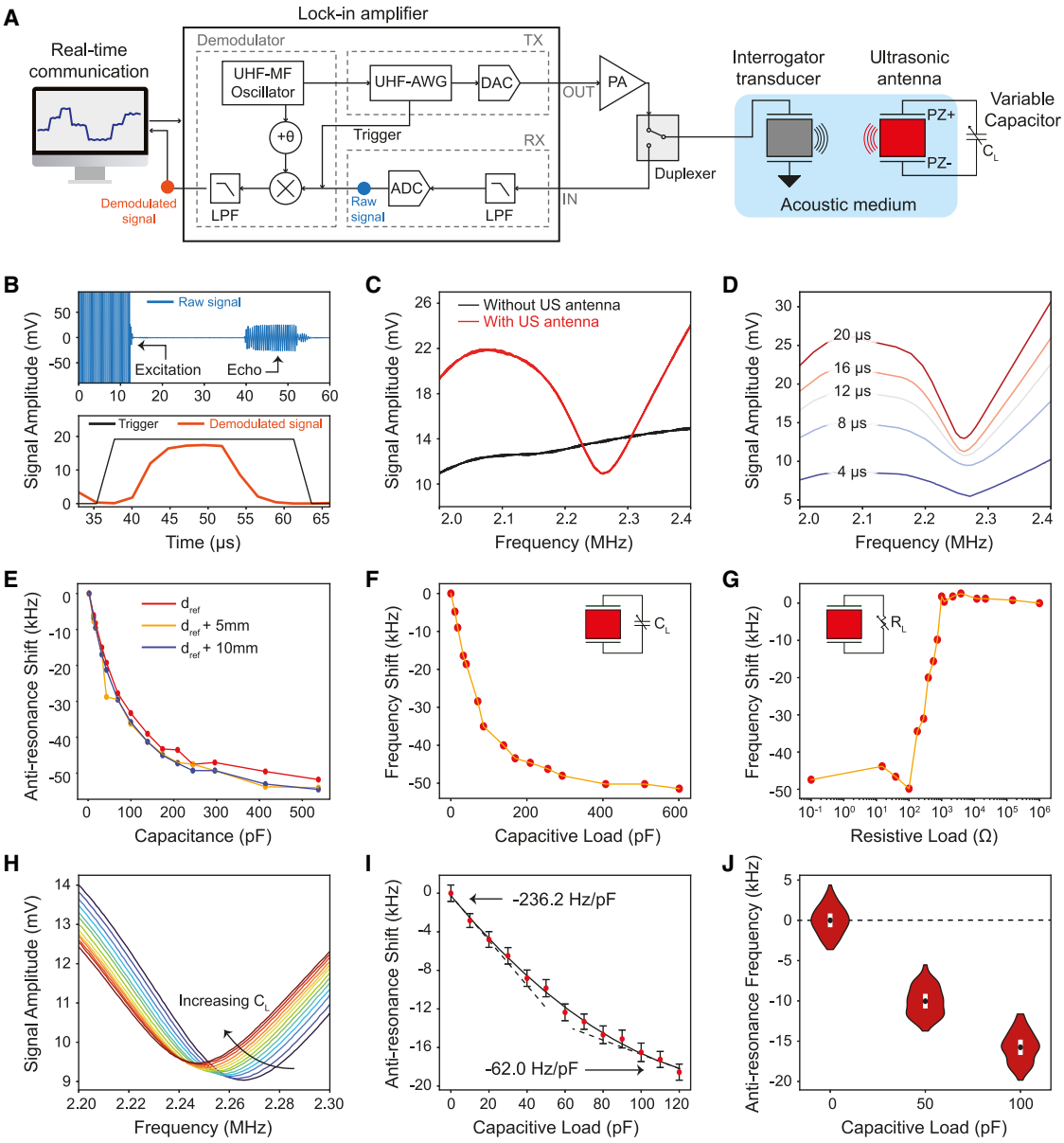


Figure 3. Communication link characterization

(A) Schematic of the wireless communication hardware block diagram. The pulse-echo operation is enabled by using a duplexer box, and the signal processing is handled by a lock-in amplifier.

(B) The raw and demodulated time-domain waveforms of a pulse-echo operation. The lock-in amplifier calculates the signal level of the echo by averaging the data points within the demodulator trigger interval. The system repeats this process for every frequency within the specified interval and forms a frequency amplitude spectrum.

(C) The acquired frequency spectrum when the US antenna is in front of the interrogator transducer is compared with the spectrum acquired without the US antenna (n = 10 measurements).

(D) The effect of the excitation signal length on the communication sweep profile.

(E) Anti-resonance shifts acquired for various antenna-transducer distances.

(F and G) The frequency shifts when capacitive (F) and resistive (G) loads are connected to the US antenna (a 10 × 10 mm^2 US antenna was used for E–G, n = 3 measurements).

(H) Frequency spectrums acquired by the passive ultrasonic communication method for varying capacitive load connected to the antenna.

(I) The frequency of the valley (anti-resonance) shifts as the load capacitance increases. Error bars represent the standard deviation (n = 50 measurements).

(J) Violin plot of the wireless communication method showing the precision of the communication link. The mean and standard deviation of the measurements are shown with white points and black bars, respectively (n = 100 measurements).

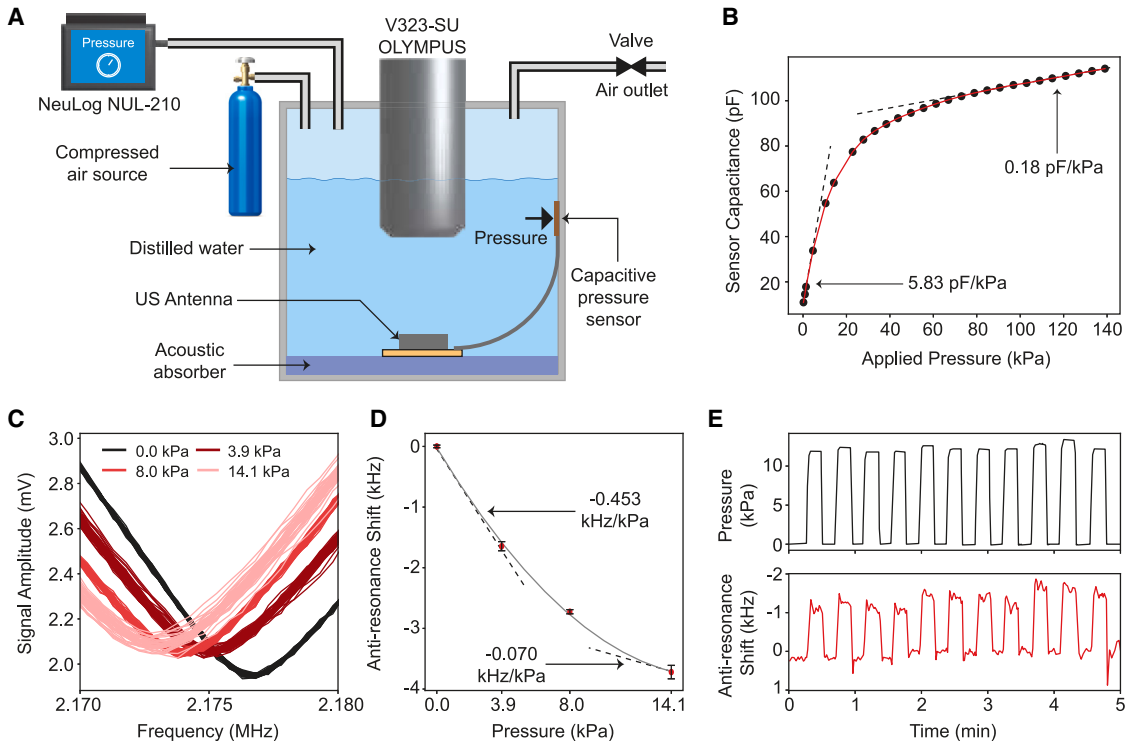


Figure 4. *In vitro* demonstration of the PUC system

(A) The schematic of the *in vitro* experimental setup showing the compressed air connections, the interrogator transducer and US antenna, the integrated capacitive pressure sensor, and the reference air pressure sensor.

(B) The capacitance plot of the integrated capacitive pressure sensor under varying pressures.

(C) Communication sweep curves for four pressure levels before applying post-processing (n = 40 measurements).

(D) The valley frequency shifts yield a sensitivity of approximately −1.07 kHz/kPa. Error bars represent the standard deviation (n = 40 measurements).

(E) Cyclic performance of the communication method. The pressure in the tank was varied manually by controlling the compressed air valve. The communication sweeps were recorded in real time with a sample rate of 1 Hz. The anti-resonance shift in the cyclic test was less than anticipated due to transverse and angular misalignment effects between the transducer and the US antenna.

can be extracted from the time of flight of the pulse-echo measurements. Moreover, the effect of resistive loads on the communication sweep results was analyzed in Figures 4F, 4G, and S5. The results suggest that capacitive load is mainly responsible for the shifts, and the resistive effects work in conjunction as described in Note S2.

Figures 3H and 3I show the PUC sweep results for various capacitive loads connected to the US antenna in parallel. As the load capacitance increases from 0 to 120 pF, the valley in the backscattered US wave spectrum experiences a total shift of 18.56 kHz. The average standard deviation for measurements was calculated to be 1.71 kHz. A second-order polynomial curve fit reveals sensitivities of 236 and 62 Hz/pF around 0 and 120 pF, respectively. Figure 3J shows a violin plot representing the distribution of the measured anti-resonance frequencies for three capacitive load values, showing decent precision.

The system can operate at a depth of at least 15 cm, as the maximum operating depth test results show in Figure S6. While distance variations have a minimal effect on the operation of the passive communication system, misalignments affect the sweep profiles and alter the anti-resonance frequencies detected by the interrogator transducer, as shown in Figure S7.

In vitro demonstration of the PUC system

To demonstrate the applicability of the PUC system, a commercial sensor was integrated with the US antenna, which was then placed in a custom-designed pressure tank. Figure 4A shows the schematic of the *in vitro* experimental setup, and Figure S8 shows the optical image of the setup. The air inlet and outlet ports of the tank were controlled manually to achieve the desired air pressure, while a reference air pressure sensor was used to monitor the air pressure inside. The tank was partially filled with distilled water to facilitate US wave propagation between the interrogator transducer and the US antenna, which were 5 cm apart.

The capacitance of the integrated commercial sensor was measured under varying pressure levels (Figure 4B), showing a sensitivity of approximately 5.83 pF/kPa at pressures below 20 kPa. Using the integrated system consisting of a US antenna and sensor, the air pressure inside the tank was monitored using the electronics-free PUC method and compared to the reference pressure sensor readings. Figure 4C shows the communication sweeps performed at four different pressure levels before any post-processing steps, showing decent separation and precision. Moreover, Figure 4D shows the mean and standard deviation of the anti-resonance frequencies extracted from the

communication sweeps. Additionally, the cyclic air pressure measurement results presented in Figure 4E show the transient performance of the PUC method. During the transient experiment, the proposed system utilized a sweep resolution of 500 Hz, resulting in a sample rate of approximately 1 Hz, limited by the hardware, as discussed in the methods section. Overall, the PUC method results demonstrate decent agreement with the pressure measured by the commercial reference sensor, as shown in Video S1.

To investigate the effect of soft tissue instead of deionized (DI) water as the acoustic medium, various acoustic media were simulated using LTspice software, including water, breast, fat, and kidney tissues of the same length (see Note S4 and Figure S9 for details). While the amplitude of the received signal decreases due to more aggressive acoustic attenuation in soft tissues compared to water, no visible change was observed in the anti-resonance frequency shifts.

Conclusion and outlook

In this work, we presented a simple, wireless, and passive frequency-based ultrasonic communication method for deep-tissue sensor implants. The method utilizes US waves and leverages the changes in the resonance characteristics of the implanted US antenna in order to facilitate communication at greater implantation depths. The system consists of a single piezoceramic US antenna connected to a capacitive sensor in parallel. We demonstrated the performance of the method *in vitro* at a depth of 5 cm by integrating a commercial capacitive pressure sensor using hydrostatic pressures ranging from 0 to 105 mmHg, showing that the device can function within the medically relevant pressure range.[50–53]

Compared to existing technologies that use US for establishing wireless communication links,[30–43] the PUC method offers several advantages (see Table S1 for a detailed comparison). First, the proposed method features only a single piezoceramic element, used as an ultrasonic antenna, soldered on a flexible conductive substrate. This enables simpler fabrication without needing any microfabrication processes. Second, the PUC system eliminates the need for custom-designed ICs and other power-harvesting electronic components, which simplifies the implant design. Finally, the PUC method offers versatile sensor integration since any sensor with capacitive sensing behavior (such as capacitive pressure and strain sensors for cardiovascular and ocular applications[14,54,55]) can be used in conjunction with the US antenna.

We observed that sweep results are affected by the misalignments between the antenna and the interrogator transducer. This can be addressed by developing pseudo-smart algorithms for transducer alignment strategies and generalized calibration methods that can diminish misalignment susceptibility. In addition, the US antenna is fabricated from PZT, a material that contains lead. Although biocompatibility is critical for implantable systems, these concerns were not prioritized for this proof-of-concept work. However, lead-free alternatives like KNN[56] can be used to fabricate the US antenna in future work. Furthermore, the antenna can be miniaturized using microfabrication processes to minimize tissue damage risks during implantation, and the sensor and antenna can be fabricated on the same substrate to achieve a monolithic implantable device. On the data processing side, the delay between the excitation and echo becomes only a few tens of microseconds, which limits the excitation duration to prevent overlap. Capturing the echo's envelope that expends over such short durations necessitates fast data conversion, demodulation, data transfer, and frequency determination. We anticipate that increasing the speed of these communication steps could lead to better signal quality, boosting the sensing precision and increasing the measurement speed beyond 2 Hz per frequency sweep. Alternative frequency sensing methods, such as band excitation using frequency chirps and pulse excitations, can increase the frequency sweep rate to as high as 1 kHz, limited only by the pulse repetition frequency of the system (Note S5; Figure S10). As a preliminary work, chirp excitation was tested with promising results, as shown in Figure S11.

METHODS

Ultrasonic antenna fabrication

A 1-mm-thick bulk PZT plate (material APC-855) was purchased from American Piezo (USA). To achieve the desired dimensions, the PZT plate was diced using a wafer dicer (DAD3221, DISCO, Japan). The 200-μm-thick flexible conductive substrate, ML-104, was purchased from LPKF. The substrate was patterned, and a 2.6 × 2.6 mm^2 area was cut for air-backing design using an R4 laser machining device (LPKF Laser & Electronics, Germany). The top and bottom electrodes of the diced PZT crystal were soldered manually to the copper pads on the patterned ML-104 substrate using a low-temperature solder (TS391LT, Chip Quik, USA). The air cavity at the back of the PZT crystal was sealed by placing Kapton tape (3M, USA) on the back of the flexible substrate. After electrical connections between the US antenna and the capacitive sensor were established, the device was coated with Parylene-C (PPS Labcoater Series 100, Germany) for an hour, creating a 900-nm-thick conformal encapsulation for electrical and chemical isolation.

Device characterization

The electrical and acoustic characterizations were performed in a distilled water environment. An impedance analyzer (MFIA, Zurich Instruments, Switzerland) was used to acquire the frequency-dependent complex electrical impedance of the US antenna. A 0.5 mm needle hydrophone (Precision Acoustics, UK) was used for the acoustic characterizations. An arbitrary waveform generator (33521B Waveform Generator, Keysight, USA) was used to excite the US antenna, while a motorized ultrasonic measurement system (UMS Research, Precision Acoustics, UK) controlled the position of the needle hydrophone connected to a digital oscilloscope (DSOX3024G, Keysight). The acoustic pressure field scan was carried out on 25 × 25 grid points with 0.4 mm increments. Figure 2H shows the interpolated version of the 25 × 25 data. The depth of the operation experiment was performed at a maximum distance of 15 cm due to the physical limitations of the experimental setup.

Communication method characterizations

The characterization tests of the PUC method were conducted in a distilled water environment using a commercial immersion transducer (V323-SU, Olympus, USA) as the interrogator

transducer. The load capacitance on the US antenna was varied by connecting the antenna to a variable capacitor (PPZN60100, Passive Plus, USA). The capacitance of the variable capacitor was measured by an impedance analyzer (MFIA, Zurich Instruments) after each adjustment. The excitation and signal processing operations of the communication sweeps were done by a LIA equipped with arbitrary waveform generator (AWG) capability (UHFLI, Zurich Instruments). A duplexer box (RDX-6, RITEC, USA) was used to enable the pulse-echo operations. The post-processing was done using Python scripts.

Communication method scheme

The signal output channel of the LIA is connected to an RF power amplifier (F30PV, Pendulum, USA) whose output port is connected to the duplexer box via a BNC cable. The receiver signal port of the duplexer is directly connected to the LIA input signal channel.

The pulse-echo scheme is realized using the LIA, which facilitates an AWG module to create 12-μs-long modulated electrical pulses to drive the interrogator transducer. An internal oscillator determines the modulation frequency. The device's echo is demodulated using this oscillator as well. This scheme allows sweeping the oscillator frequency while keeping the measurement and pulse modulation in sync. The frequency sweep is performed in the vicinity of the anticipated anti-resonance frequency. At each frequency point, the signal is demodulated using a fourth-order low-pass filter with 200 kHz cutoff frequency. The resulting signal is the envelope of the modulated signal corresponding to the backscattered wave, as shown in Figure 3B. The control software calculates the average amplitude and plots it against the frequency. The sweep results are continuously fed into a Python script, which applies a 1D Gaussian filter to smooth the spectrum before outputting the frequency of the anti-resonance valley (Figure S12).

In vitro demonstration of the communication method

The *in vitro* experimental setup was constructed using a 15 × 15 × 15 cm^3 polycarbonate box and a 3D-printed top cover, which holds the interrogator transducer and facilitates the air hose connections. Rubber O-rings were used to seal the box and prevent air leakages. A total of three air hose connections were designed: one for the air inlet, one for the air outlet, and one for the reference air pressure sensor readings.

The commercial pressure sensor (FlexiForce A201, Tekscan, USA) was integrated with the fabricated US antenna, and the integrated device was placed inside the box so that the US antenna would be directly under the interrogator transducer. The sensing area of the commercial pressure sensor was fixed on the box wall. The reference pressure readings were taken by a reference air pressure sensor (NUL210, NeuLog, USA).

RESOURCE AVAILABILITY

Lead contact

Further information and resource requests should be directed to the corresponding author, Levent Beker (lbeker@ku.edu.tr).

Materials availability

The materials used in this study are commercially available and can be purchased from the sources listed in the methods section.

Data and code availability

The datasets and code can be obtained by contacting the authors via email.

ACKNOWLEDGMENTS

U.C.Y. is supported by the Scientific and Technological Research Council of Turkey (TUBITAK) through the 2210/A program. A.T.T. is supported by through the TUBITAK 2232 (grant no. 118C295) program. L.B. acknowledges TUBITAK 2232 (grant no. 118C295) and the European Research Council (grant no. 101043119). We acknowledge the Koç University Nanofabrication and Nanocharacterization Center (n2STAR) for access to the infrastructure.

AUTHOR CONTRIBUTIONS

U.C.Y. and L.B. conceived the research idea. U.C.Y. designed, fabricated, and characterized the ultrasonic antenna, conducted experiments, and analyzed the data. A.T.T. contributed to the experiments and technical discussions. K.E. and M.A. contributed to signal processing. L.B. acquired funding and directed the research activities. All authors contributed to the manuscript writing.

DECLARATION OF INTERESTS

L.B. is the inventor of the patent (WO2023018388A1) that covers the fundamental principles of the passive communication method.

SUPPLEMENTAL INFORMATION

Supplemental information can be found online at https://doi.org/10.1016/j.device.2025.100755.

Received: October 15, 2024
Revised: December 10, 2024
Accepted: March 5, 2025
Published: March 28, 2025

REFERENCES

1. Maday, K.R., Hurt, J.B., Harrelson, P., and Porterfield, J. (2016). Evaluating postoperative fever. JAAPA *29*, 23–28. https://doi.org/10.1097/01.JAA.0000496951.72463.de.
2. Hoffmann, J., Mollan, S.P., Paemeleire, K., Lampl, C., Jensen, R.H., and Sinclair, A.J. (2018). European Headache Federation guideline on idiopathic intracranial hypertension. J. Headache Pain *19*, 93. https://doi.org/10.1186/s10194-018-0919-2.
3. Hunter, J.D., and Damani, Z. (2004). Intra-abdominal hypertension and the abdominal compartment syndrome. Anaesthesia *59*, 899–907. https://doi.org/10.1111/j.1365-2044.2004.03712.x.
4. Kobayashi, H., Longmire, M.R., Ogawa, M., Choyke, P.L., and Kawamoto, S. (2010). Multiplexed imaging in cancer diagnosis: applications and future advances. Lancet Oncol. *11*, 589–595. https://doi.org/10.1016/S1470-2045(10)70009-7.
5. Bidot, S., Saindane, A.M., Peragallo, J.H., Bruce, B.B., Newman, N.J., and Biousse, V. (2015). Brain Imaging in Idiopathic Intracranial Hypertension. J. Neuroophthalmol. *35*, 400–411. https://doi.org/10.1097/WNO.0000000000000303.
6. Pelosi, P., Aspesi, M., Gamberoni, C., Chiumello, D., Severgnini, P., Oggioni, R., Tulli, G., Malacrida, R., and Chiaranda, M. (2002). Measuring intra-abdominal pressure in the intensive care setting. Intensivmed *39*, 509–519. https://doi.org/10.1007/s00390-002-0312-9.
7. Abraham, M., and Singhal, V. (2018). Intracranial pressure monitoring. J. Neuroanaesth. Crit. Care *2*, 193–203. https://doi.org/10.4103/2348-0548.165039.

8. Smith, M. (2008). Monitoring Intracranial Pressure in Traumatic Brain Injury. Anesth. Analg. *106*, 240–248. https://doi.org/10.1213/01.ane.0000297296.52006.8e.

9. Feneley, R.C.L., Hopley, I.B., and Wells, P.N.T. (2015). Urinary catheters: history, current status, adverse events and research agenda. J. Med. Eng. Technol. *39*, 459–470. https://doi.org/10.3109/03091902.2015.1085600.

10. Hanna, R., and Raad, I.I. (2005). Diagnosis of catheter-related bloodstream infection. Curr. Infect. Dis. Rep. *7*, 413–419. https://doi.org/10.1007/s11908-005-0042-9.

11. Lange, R.A., and Hillis, L.D. (2003). Diagnostic Cardiac Catheterization. Circulation *107*, e111–e113. https://doi.org/10.1161/01.CIR.0000070982.94049.A2.

12. Dellimore, K.H., Helyer, A.R., and Franklin, S.E. (2013). A scoping review of important urinary catheter induced complications. J. Mater. Sci. Mater. Med. *24*, 1825–1835. https://doi.org/10.1007/s10856-013-4953-y.

13. Bouza, E., Burillo, A., and Muñoz, P. (2002). Catheter-related infections: diagnosis and intravascular treatment. Clin. Microbiol. Infect. *8*, 265–274. https://doi.org/10.1046/j.1469-0691.2002.00385.x.

14. Boutry, C.M., Beker, L., Kaizawa, Y., Vassos, C., Tran, H., Hinckley, A.C., Pfattner, R., Niu, S., Li, J., Claverie, J., et al. (2019). Biodegradable and flexible arterial-pulse sensor for the wireless monitoring of blood flow. Nat. Biomed. Eng. *3*, 47–57. https://doi.org/10.1038/s41551-018-0336-5.

15. Rodriguez, S., Ollmar, S., Waqar, M., and Rusu, A. (2016). A Batteryless Sensor ASIC for Implantable Bio-Impedance Applications. IEEE Trans. Biomed. Circuits Syst. *10*, 533–544. https://doi.org/10.1109/TBCAS.2015.2456242.

16. Herbert, R., Mishra, S., Lim, H.-R., Yoo, H., and Yeo, W.-H. (2019). Fully Printed, Wireless, Stretchable Implantable Biosystem toward Batteryless, Real-Time Monitoring of Cerebral Aneurysm Hemodynamics. Adv. Sci. *6*, 1901034. https://doi.org/10.1002/advs.201901034.

17. Hu, S., Chen, H., Jia, S., Xiao, X., Cao, Y., and Wang, W. (2021). A wireless passive extra-arterial implantable blood pressure monitoring sensing system for rats. Microsyst. Technol. *27*, 2595–2603. https://doi.org/10.1007/s00542-020-05011-4.

18. Zhang, H., Gutruf, P., Meacham, K., Montana, M.C., Zhao, X., Chiarelli, A.M., Vázquez-Guardado, A., Norris, A., Lu, L., Guo, Q., et al. (2019). Wireless, battery-free optoelectronic systems as subdermal implants for local tissue oximetry. Sci. Adv. *5*, eaaw0873. https://doi.org/10.1126/sciadv.aaw0873.

19. Vassiliou, C.C., Liu, V.H., and Cima, M.J. (2015). Miniaturized, biopsy-implantable chemical sensor with wireless, magnetic resonance readout. Lab Chip *15*, 3465–3472. https://doi.org/10.1039/C5LC00546A.

20. Wang, W., Pradhan, R., Ho, Y.S., Zhao, Z., Sun, Q., Liao, X., Wang, S., Fang, Z., and Zheng, Y. (2021). MRC-Based Double Figure-of-Eight Coil Sensor System With Triple-Mode Operation Capability for Biomedical Applications. IEEE Sens. J. *21*, 14491–14502. https://doi.org/10.1109/JSEN.2020.3020578.

21. Kang, S.-K., Murphy, R.K.J., Hwang, S.-W., Lee, S.M., Harburg, D.V., Krueger, N.A., Shin, J., Gamble, P., Cheng, H., Yu, S., et al. (2016). Bioresorbable silicon electronic sensors for the brain. Nature *530*, 71–76. https://doi.org/10.1038/nature16492.

22. Yamagishi, K., Zhou, W., Ching, T., Huang, S.Y., and Hashimoto, M. (2021). Ultra-Deformable and Tissue-Adhesive Liquid Metal Antennas with High Wireless Powering Efficiency. Adv. Mater. *33*, 2008062. https://doi.org/10.1002/adma.202008062.

23. Vennemann, B., Obrist, D., and Rösgen, T. (2020). A smartphone-enabled wireless and batteryless implantable blood flow sensor for remote monitoring of prosthetic heart valve function. PLoS One *15*, e0227372. https://doi.org/10.1371/journal.pone.0227372.

24. Kwon, K., Kim, J.U., Won, S.M., Zhao, J., Avila, R., Wang, H., Chun, K.S., Jang, H., Lee, K.H., Kim, J.-H., et al. (2023). A battery-less wireless implant for the continuous monitoring of vascular pressure, flow rate and temperature. Nat. Biomed. Eng. *7*, 1215–1228. https://doi.org/10.1038/s41551-023-01022-4.

25. Silemek, B., Acikel, V., Oto, C., Alipour, A., Aykut, Z.G., Algin, O., and Atalar, E. (2018). A temperature sensor implant for active implantable medical devices for in vivo subacute heating tests under MRI. Magn. Reson. Med. *79*, 2824–2832. https://doi.org/10.1002/mrm.26914.

26. Wu, T., Redouté, J.-M., and Yuce, M.R. (2018). A Wireless Implantable Sensor Design With Subcutaneous Energy Harvesting for Long-Term IoT Healthcare Applications. IEEE Access *6*, 35801–35808. https://doi.org/10.1109/ACCESS.2018.2851940.

27. Chamis, A.L., Peterson, G.E., Cabell, C.H., Corey, G.R., Sorrentino, R.A., Greenfield, R.A., Ryan, T., Reller, L.B., and Fowler, V.G. (2001). Staphylococcus aureus Bacteremia in Patients With Permanent Pacemakers or Implantable Cardioverter-Defibrillators. Circulation *104*, 1029–1033. https://doi.org/10.1161/hc3401.095097.

28. Hall-Stoodley, L., Costerton, J.W., and Stoodley, P. (2004). Bacterial biofilms: from the Natural environment to infectious diseases. Nat. Rev. Microbiol. *2*, 95–108. https://doi.org/10.1038/nrmicro821.

29. Thimot, J., and Shepard, K.L. (2017). Bioelectronic devices: Wirelessly powered implants. Nat. Biomed. Eng. *1*, 0051. https://doi.org/10.1038/s41551-017-0051.

30. Seo, D., Neely, R.M., Shen, K., Singhal, U., Alon, E., Rabaey, J.M., Carmena, J.M., and Maharbiz, M.M. (2016). Wireless Recording in the Peripheral Nervous System with Ultrasonic Neural Dust. Neuron *91*, 529–539. https://doi.org/10.1016/j.neuron.2016.06.034.

31. Ozeri, S., and Shmilovitz, D. (2010). Ultrasonic transcutaneous energy transfer for powering implanted devices. Ultrasonics *50*, 556–566. https://doi.org/10.1016/j.ultras.2009.11.004.

32. Johnson, B.C., Shen, K., Piech, D., Ghanbari, M.M., Li, K.Y., Neely, R., Carmena, J.M., Maharbiz, M.M., and Muller, R. (2018). StimDust: A 6.5mm3, wireless ultrasonic peripheral nerve stimulator with 82% peak chip efficiency. In 2018 IEEE Custom Integrated Circuits Conference (CICC) (IEEE), pp. 1–4. https://doi.org/10.1109/CICC.2018.8357047.

33. Piech, D.K., Johnson, B.C., Shen, K., Ghanbari, M.M., Li, K.Y., Neely, R.M., Kay, J.E., Carmena, J.M., Maharbiz, M.M., and Muller, R. (2020). A wireless millimetre-scale implantable neural stimulator with ultrasonically powered bidirectional communication. Nat. Biomed. Eng. *4*, 207–222. https://doi.org/10.1038/s41551-020-0518-9.

34. Shi, C., Costa, T., Elloian, J., Zhang, Y., and Shepard, K.L. (2020). A 0.065-mm ^{3} Monolithically-Integrated Ultrasonic Wireless Sensing Mote for Real-Time Physiological Temperature Monitoring. IEEE Trans. Biomed. Circuits Syst. *14*, 412–424. https://doi.org/10.1109/TBCAS.2020.2971066.

35. Sonmezoglu, S., Fineman, J.R., Maltepe, E., and Maharbiz, M.M. (2021). Monitoring deep-tissue oxygenation with a millimeter-scale ultrasonic implant. Nat. Biotechnol. *39*, 855–864. https://doi.org/10.1038/s41587-021-00866-y.

36. Charthad, J., Weber, M.J., Chang, T.C., and Arbabian, A. (2015). A mm-Sized Implantable Medical Device (IMD) With Ultrasonic Power Transfer and a Hybrid Bi-Directional Data Link. IEEE J. Solid-State Circuits *50*, 1741–1753. https://doi.org/10.1109/JSSC.2015.2427336.

37. Maleki, T., Cao, N., Song, S.H., Kao, C., Ko, S.C.A., and Ziaie, B. (2011). An Ultrasonically Powered Implantable Micro-Oxygen Generator (IMOG). IEEE Trans. Biomed. Eng. *58*, 3104–3111. https://doi.org/10.1109/TBME.2011.2163634.

38. Larson, P.J., and Towe, B.C. (2011). Miniature ultrasonically powered wireless nerve cuff stimulator. In 2011 5th International IEEE/EMBS Conference on Neural Engineering (IEEE), pp. 265–268. https://doi.org/10.1109/NER.2011.5910538.

39. Maini, L., Genovés, V., Furrer, R., Cesarovic, N., Hierold, C., and Roman, C. (2024). An in vitro demonstration of a passive, acoustic metamaterial as a temperature sensor with mK resolution for implantable applications. Microsyst. Nanoeng. *10*, 1–14. https://doi.org/10.1038/s41378-023-00632-x.

40. Zang, J., Tian, Y., Yang, Y., Tang, H., Wang, J., Cheng, Y., Kang, T., Li, N., Zhou, M., Chen, W., et al. (2023). An electronics-free implant for continuous and wireless monitoring of internal tissue strains. Preprint at Res. Sq. https://doi.org/10.21203/rs.3.rs-3094476/v1.

41. Barri, K., Zhang, Q., Swink, I., Aucie, Y., Holmberg, K., Sauber, R., Altman, D.T., Cheng, B.C., Wang, Z.L., and Alavi, A.H. (2022). Patient-Specific Self-Powered Metamaterial Implants for Detecting Bone Healing Progress. Adv. Funct. Mater. *32*, 2203533. https://doi.org/10.1002/adfm.202203533.

42. Tang, H., Yang, Y., Liu, Z., Li, W., Zhang, Y., Huang, Y., Kang, T., Yu, Y., Li, N., Tian, Y., et al. (2024). Injectable ultrasonic sensor for wireless monitoring of intracranial signals. Nature *630*, 84–90. https://doi.org/10.1038/s41586-024-07334-y.

43. Mutlu, S., Aghakhani, A., and Sitti, M. (2022). Piezo Capsule: Ultrasonic Way of Wireless Pressure Measurement. Adv. Intell. Syst. *4*, 2200125. https://doi.org/10.1002/aisy.202200125.

44. Hong, C.-H., Kim, H.-P., Choi, B.-Y., Han, H.-S., Son, J.S., Ahn, C.W., and Jo, W. (2016). Lead-free piezoceramics – Where to move on? J. Materiomics *2*, 1–24. https://doi.org/10.1016/j.jmat.2015.12.002.

45. Jirik, R., Taxt, T., and Jan, J. (2004). Estimation of ultrasound attenuation coefficient using log-spectrum domain processing. In The 26th Annual International Conference of the IEEE Engineering in Medicine and Biology Society (IEEE), pp. 1411–1414. https://doi.org/10.1109/IEMBS.2004.1403438.

46. Mason, W.P. (1964). Electromechanical transducers and wave filters (D. Van Nostrand Co).

47. Castillo, M., Acevedo, P., and Moreno, E. (2003). KLM model for lossy piezoelectric transducers. Ultrasonics *41*, 671–679. https://doi.org/10.1016/S0041-624X(03)00101-X.

48. Redwood, M. (1961). Transient Performance of a Piezoelectric Transducer. J. Acoust. Soc. Am. *33*, 527–536. https://doi.org/10.1121/1.1908709.

49. Sherrit, S., and Mukherjee, B.K. (2007). Characterization of Piezoelectric Materials for Transducers. Preprint at arXiv. https://doi.org/10.48550/arXiv.0711.2657.

50. Czosnyka, M., and Pickard, J.D. (2004). Monitoring and interpretation of intracranial pressure. J. Neurol. Neurosurg. Psychiatry *75*, 813–821. https://doi.org/10.1136/jnnp.2003.033126.

51. Malbrain, M.L.N.G., Cheatham, M.L., Kirkpatrick, A., Sugrue, M., Parr, M., De Waele, J., Balogh, Z., Leppäniemi, A., Olvera, C., Ivatury, R., et al. (2006). Results from the International Conference of Experts on Intra-abdominal Hypertension and Abdominal Compartment Syndrome. I. Definitions. Intensive Care Med. *32*, 1722–1732. https://doi.org/10.1007/s00134-006-0349-5.

52. Galiè, N., Hoeper, M.M., Humbert, M., Torbicki, A., Vachiery, J.-L., Barbera, J.A., Beghetti, M., Corris, P., Gaine, S., Gibbs, J.S., et al. (2009). Guidelines for the diagnosis and treatment of pulmonary hypertension: The Task Force for the Diagnosis and Treatment of Pulmonary Hypertension of the European Society of Cardiology (ESC) and the European Respiratory Society (ERS), endorsed by the International Society of Heart and Lung Transplantation (ISHLT). Eur. Heart J. *30*, 2493–2537. https://doi.org/10.1093/eurheartj/ehp297.

53. Mubarak, S.J., Owen, C.A., Hargens, A.R., Garetto, L.P., and Akeson, W.H. (1978). Acute compartment syndromes: diagnosis and treatment with the aid of the wick catheter. J. Bone Joint Surg. Am. *60*, 1091–1095.

54. Ha, D., de Vries, W.N., John, S.W.M., Irazoqui, P.P., and Chappell, W.J. (2012). Polymer-based miniature flexible capacitive pressure sensor for intraocular pressure (IOP) monitoring inside a mouse eye. Biomed. Microdevices *14*, 207–215. https://doi.org/10.1007/s10544-011-9598-3.

55. Zhang, C., Ouyang, W., Zhang, L., and Li, D. (2023). A dual-mode fiber-shaped flexible capacitive strain sensor fabricated by direct ink writing technology for wearable and implantable health monitoring applications. Microsyst. Nanoeng. *9*, 158. https://doi.org/10.1038/s41378-023-00634-9.

56. Hou, J.F., Nayeem, M.O.G., Caplan, K.A., Ruesch, E.A., Caban-Murillo, A., Criado-Hidalgo, E., Ornellas, S.B., Williams, B., Pearce, A.A., Dagdeviren, H.E., et al. (2024). An implantable piezoelectric ultrasound stimulator (ImPULS) for deep brain activation. Nat. Commun. *15*, 4601. https://doi.org/10.1038/s41467-024-48748-6.